Experimental Thermal and Fluid Science 52 (2014) 297–307

Contents lists available at ScienceDirect

Experimental Thermal and Fluid Science

journal homepage: www.elsevier.com/locate/etfs

Modulated flow patterns for vertical upflow by the phase separation concept

Hongxia Chen [a], Jinliang Xu [a,b,*], Jian Xie [b], Feng Xing [b], Zijin Li [b]

[a] The Beijing Key Laboratory of Multiphase Flow and Heat Transfer, North China Electric Power University, Beijing 102206, China
[b] The Beijing Key Laboratory of New and Renewable Energy, North China Electric Power University, Beijing 102206, PR China

ARTICLE INFO

Article history:
Received 6 June 2013
Received in revised form 18 September 2013
Accepted 24 September 2013
Available online 18 October 2013

Keywords:
Multiphase flow
Heat transfer
Bubble
Phase change
Flow pattern
Mesh pore surface

ABSTRACT

The passive phase separation concept was proposed to create thin liquid film on the wall surface. The inserted mesh cylinder made of a single layer of mesh pore surface divides the tube cross section into an annular region near the tube wall and a core region. Gas bubbles are prevented from entering the core region and liquids can be sucked towards the core region. Thus, the two-phases are majorly flowing in two different regions. The concept is expected to be used for multiphase (boiling/evaporation and condensation) heat transfer enhancement. Air–water two-phase flow experiments were performed with vertical upflows. Miniature bubbles are modulated to flow in the annular region. Cap/slug/plug bubbles are modulated to form the elongated-ring-slug bubble in the annular region to generate thin liquid films on the wall. For all the cases, the core region is full of liquid. Due to the large density difference between liquid in the core region and gas in the annular region, pulsating flow is self-sustained in the core region. The mesh pore surface promotes the mass and momentum exchange between the annular region and core region. For ring-slug bubbles such as longer than 10 cm, miniature bubbles are emitted from the slug bubble front. The proposed concept is being verified by the phase change heat transfer experiment in our laboratory.

1. Introduction

Boiling/evaporation and condensation are natural phenomena and widely applied in various industry sectors [1]. Even though these topics have been studied for more than one century, the complicated mechanisms are not fully understood. Recently, due to the energy shortage and environmental problem, low grade energy utilization becomes a hot area attracting scientists and engineers. The Orgainc Rankine Cycle is one of the solutions to recover the low grade energy including waste heat, solar thermal energy and geothermal energy, etc. [2]. In such a system, an evaporator generates vapor to drive turbine for the power generation, and a condenser cools the vapor to liquid. Both evaporator and condenser are phase change heat transfer components. From the thermodynamic cycle point of view, small temperature differences across the two sides of fluids result in small exergy loss and high efficiency, causing a good system performance to achieve large power output. For a desired heat to be received by the evaporator or dissipated by the condenser, large heat transfer coefficients are required to avoid non-acceptable large heat transfer area at low temperature difference across the two sides of fluids. This is especially important because the phase change heat transfer coefficients are not high when organic fluids are used. For instance, for a water cooled condenser, the condensation heat transfer coefficient with organic fluid is ~1 kW/m^2 K [3], which may be smaller than that for the cooling water flowing in the tube annulus.

The conventional multiphase heat transfer enhancement uses heat transfer tubes with microstructures on the wall. The helically corrugated tubes [3], micro groove tubes [4], micro-fin tubes [5] and herringbone tubes [6] are examples of these tubes. The heat transfer coefficient can be increased by mixing the fluid boundary layers and also by limiting the growth of fluid boundary layers close to the heat transfer surfaces.

For multiphase heat transfer, the key scientific issue is the synergy (coordination) of the flow pattern and heat transfer characteristic. It is well known that void fractions are larger at the tube centerline and smaller near the tube wall. In other words, gas tends to be in the tube core and liquid tends to be near the tube wall. This phase distribution involves thick liquid film thickness near the tube wall to deteriorate heat transfer. The conventional hest transfer tubes do not coordinate the flow pattern with the heat transfer performance. Lips and Meyer [7] experimentally investigated the convective condensation of R134a in an 8.38 mm inclined smooth

* Corresponding author at: The Beijing Key Laboratory of Multiphase Flow and Heat Transfer, North China Electric Power University, Beijing 102206, China. Tel./fax: +86 10 61772268.
E-mail address: xjl@ncepu.edu.cn (J. Xu).

0894-1777/$ - see front matter © 2013 Elsevier Inc. All rights reserved.
http://dx.doi.org/10.1016/j.expthermflusci.2013.09.021

Nomenclature

A	tube cross section area (m^2)
A_a	cross sectional area of the annular region (m^2)
$A_{mesh\text{-}cylinder}$	the total mesh pore area over a slug bubble height (m^2)
Ca	capillary number
D	tube diameter (m)
D_{eff}	effect diameter of the annular region (m)
D	mesh cylinder diameter (m)
d_{eff}	effective mesh pore size (m)
g	gravity acceleration (m/s^2)
h	heat transfer coefficient (w/m^2 k)
k_l	liquid thermal conductivity (w/m k)
J	superficial velocity (m/s)
L_s	length of the slug bubble (m)
$L_{s,c}$	critical bubble length (m)
$L_{s,\max}$	maximum slug bubble length (m)
L_l	length of the liquid plug (m)
m_p	mass exchange between the annular region and core region around a single slug bubble (kg/s)
P	pressure (Pa)
Q	volume flow rate (m^3/s)
r	radial coordinate (m)
Re	Reynolds number
St	Strouhal number
U	bubble velocity (m/s)
U_p	pulsating flow velocity induced by the buoyancy force (m/s)
W	annular gap size (m)
w	mesh pore width (m)
x	coordinate along the flow direction (m)
x_t	locally attached coordinate along the flow direction in Fig. 10

Greek symbols

α	contact angle (°)
$\beta_{l,a}$	liquid volume fraction in the annular region
δ	liquid film thickness (m)
ρ_g	gas density (kg/m^3)
ρ_l	liquid density (kg/m^3)
$\Delta\rho$	density difference between liquid and gas (kg/m^3)
σ	surface tension force (N/m)
μ	viscosity (pa s)
η	liquid separation ratio by the mesh cylinder

Subscripts

buoyancy	buoyancy force
b	bubble
c	critical
g	gas
l	liquid
s	starting location
e	ending location

Abbreviation

PPI	pores per inch

tube. The flow patterns and heat transfer coefficients were presented with different mass fluxes and vapor mass qualities over the whole range of inclination angles (from vertical downwards to vertical upwards). The heat transfer coefficient is found to be strongly influenced by the liquid and vapor distributions and especially by the liquid thickness at the tube bottom for stratified flow.

For boiling heat transfer in tubes, there are two heat transfer mechanisms depending on operating parameters: the nucleate boiling heat transfer mechanism with the heat transfer coefficients influenced by heat fluxes, and the convective boiling heat transfer mechanism with the heat transfer coefficients controlled by mass fluxes. The boiling/evaporation heat transfer is also related to the phase distribution. Han et al. [8] noted that the liquid film evaporation is one of the important heat transfer mechanisms and the liquid film thickness is a very important parameter to determine the heat transfer coefficient. Many studies have been performed to measure and simulate the liquid film thickness (Han et al. [8], Han and Shikazono [9], Han and Shikazono [10], Fang et al. [11]). However, how to generate the thin liquid film on the tube wall has less been reported.

In this study, the phase separation concept was proposed to modulate the flow patterns for vertical upflows. A mesh cylinder was suspended in the heat transfer tube, dividing the tube cross section into an annular region and a core region. The mesh pore surface ensures gas bubbles flowing in the annular region and liquid flowing in the core region. Confinement of gas bubbles in the annular region results in the thin liquid film. Besides, the present paper identified the buoyancy force induced pulsating flow in the core region. The mesh pore surface creates the enhanced liquid mass and momentum exchange between the annular region and core region. Both the thin liquid film and buoyancy force induced pulsating flow are expected to enhance the multiphase heat transfer.

2. Design of the heat transfer tube

Confinement of gas bubbles in a small space creates thin liquid films. Fig. 1 shows the gas–liquid separator made of a single layer

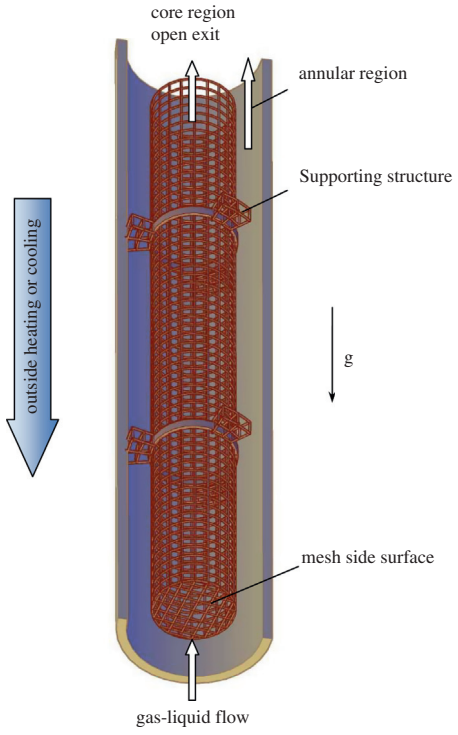

Fig. 1. The proposed heat transfer tube.

of mesh cylinder, uniformly suspended in a heat transfer tube. The supporting structure may be needed. The cross section of the heat transfer tube consists of an annular region and a core region. The mesh cylinder has a taper, or just a flat bottom mesh surface. The mesh cylinder exit is open to discharge the separated liquid. The core region is empty.

The mesh pores have two functions when a two-phase flow stream interacts with the mesh cylinder. The first function prevents gas bubbles from entering the core region. The second function sucks liquid towards the core region. Thus, the gas and liquid phases are separated to flow in the two different regions. This phase distribution is opposite of that in a conventional bare tube.

The heating and cooling boundary conditions on the outer tube wall involve the boiling/evaporation and condensation heat transfer in the tube, respectively. For the condensation heat transfer, the mesh cylinder is arranged downstream the tube entrance. The annular flow pattern at the tube entrance has a good heat transfer performance. Thus, the modulation for the annular flow is not necessary. With the flow development, the intermittent flow patterns (slug, plug, churn, bubble flows) thicken the liquid film thickness on the tube wall, deteriorating the heat transfer. The flow pattern modulation is also expected to be useful for air–water two-phase heat transfer without phase change.

Small mesh pore size prevents gas bubbles from entering the core region and pumps the liquid towards the core region. A criterion for the mesh pore size is suggested as $d_{eff} < \sqrt{\sigma/g(\rho_l - \rho_g)}$, which is on the order of millimeter for most gas–liquid systems, where σ is the surface tension force, g is the gravity, ρ_l and ρ_g are the liquid and gas densities, respectively.

Fig. 2a shows the picture of the stainless steel mesh used for this experiment. Each mesh pore had a rectangular cross section with its size of 0.15 mm by 0.15 mm. The mesh wire had a thickness of 0.07 mm. The PPI (pores per inch) of the mesh was 115. Fig. 2b and c shows the inlet part and outlet part of the fabricated mesh cylinder, respectively.

3. Experiment

3.1. The test section

Two test sections were fabricated to examine the effect of the inserted mesh cylinder on the flow patterns (see Fig. 3a and b). The deionized water entered the test section from the tube inlet

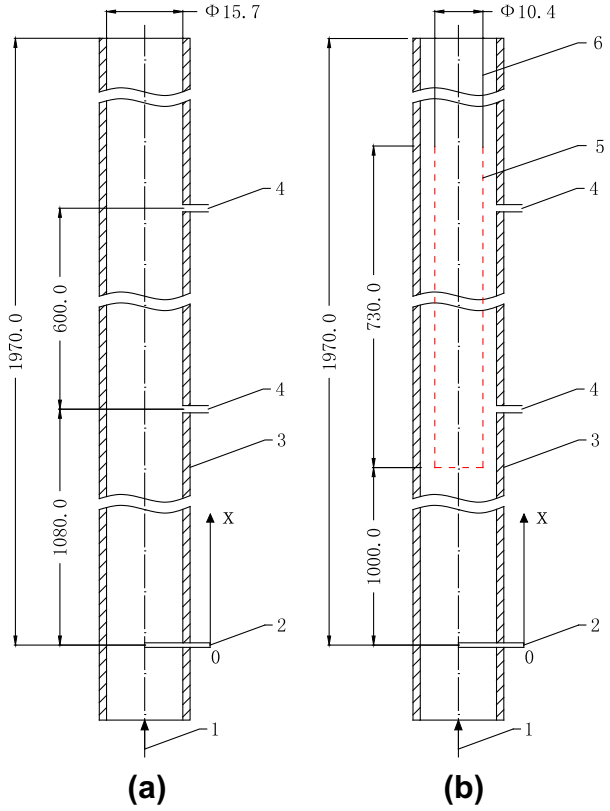

Fig. 3. The vertical tube test section (a: bare tube, b: vertical tube with a mesh cylinder inserted, 1: water inlet, 2: air inlet from needle holes, 3: glass tube, 4: pressure ports, 5: mesh cylinder, 6: two supporting lags, all dimensions are in millimeter).

(referred as 1 in Fig. 3). A set of miniature needles were distributed uniformly along the tube circumference (only one needle shown in Fig. 3). Miniature bubbles are generated periodically at the needle tip to mix with the liquid stream thoroughly, forming the desired flow pattern. In order to characterize the two-phase flow behavior along the flow direction, the x coordinate was specified with the original point at the needle location. Two pressure ports (referred as 4 in Fig. 3) were arranged along the flow direction with a distance of 600 mm between them. The first pressure port was at

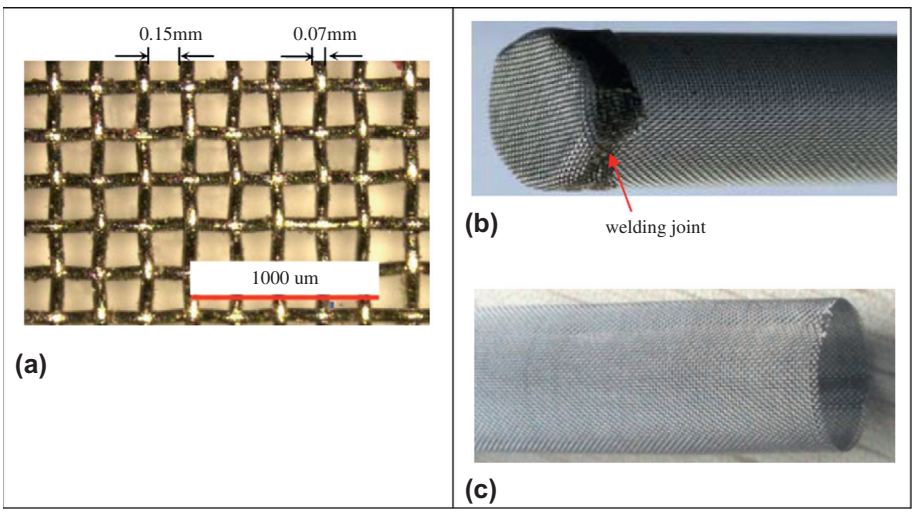

Fig. 2. The stainless steel mesh to fabricate the mesh cylinder, (a) the photo of the stainless steel mesh, (b) the fabricated mesh cylinder focusing on the inlet region and (c) the fabricated mesh cylinder focusing on the exit region.

x = 1080 mm. The two pressure ports were connected by a pressure drop transducer. Both the two test sections were made of glass so that the flow can be observed.

The glass tube had a total length of 1970 mm with an inner diameter of 15.7 mm and a tube wall thickness of 2.0 mm. For the second test section, the mesh cylinder started from x = 1000 mm with an open end. It was uniformly suspended in the glass tube by three supporting structures (not shown in Fig. 3b). The outer mesh cylinder had a diameter of 10.4 mm to form an annular gap of 2.65 mm between the mesh cylinder and the tube wall.

3.2. The experimental setup

Fig. 4 shows the experiment setup. The water flow rate was supplied by a water pump with variable rotating speeds. Solid particles were prevented from entering the pump by a filter at the pump inlet. The water flow rate was measured by one of the two turbine flowmeters, having the ranges of 0.2–2 m^3/h and 0.6–6 m^3/h, respectively. The air flow rate was provided by an air compressor and it was measured by one of the three rotameters with the ranges of 0.016–0.16 m^3/h, 0.1–1 m^3/h and 1–10 m^3/h, respectively. All the five flowmeters had accuracies of 0.5% within their own flow rate range. The pressure drop transducer had the accuracy of 0.1%. A high speed camera (HG-100 K, Redlake Inc., USA) captured the flow patterns. A software (Photoshop CS5) analyzed the image pixels to locate the exact gas–liquid interface with a resolution of 10 μm.

The test section was vertically positioned. The superficial velocities of liquid and gas phases are defined as

$$J_l = \frac{Q_l}{A},\ J_g = \frac{Q_g}{A} \tag{1}$$

where Q_l and Q_g are the volume flow rates of liquid and gas phases, A is the tube cross section area. In this experiment, J_l and J_g had the ranges of 0.01–2.0 m/s and 0.1–10 m/s, respectively.

4. Results and discussion

4.1. Flow patterns in the bare tube

Many text books on the two-phase flow and heat transfer describe the flow patterns in vertical tubes. Fig. 5 shows flow patterns in the present tube. The bubbly flow, slug flow, churn flow and annular flow were observed, which are described as follows.

(a) *Bubbly flow*. Liquids are flowing in the tube as a continuous phase while gas is distributed in the continuous liquid phase as discrete small bubbles. The flow regime occurs at large liquid velocities.
(b) *Slug flow*. An increase in the gas flow rate causes the coalescence of bubbles resulting in the formation of bullet shaped Taylor bubbles, separated by liquid-slugs usually containing small gas bubbles. The net flow is upward. The liquid between the Taylor bubbles and the tube wall flows downward in the form of a falling liquid film.
(c) *Churn flow*. Churn flow is an important regime occurring between slug and annular flows. The Taylor bubbles break through the enclosing liquid to form a gas passage in the tube centre. The video images in this regime do not have distinctive peculiarities and also represent gradual change from the images for the slug regime to annular regime.
(d) *Annular flow*. A still higher gas velocity results in the formation of a gas core with a liquid film around the tube periphery. The film may or may not be continuous around the entire circumference but it will, of course, be thicker at the base of the tube. Miniature liquid droplets may be entrained in the gas core. The wispy annular flow regime occurs at higher liquid velocities with wavy gas–liquid interface.

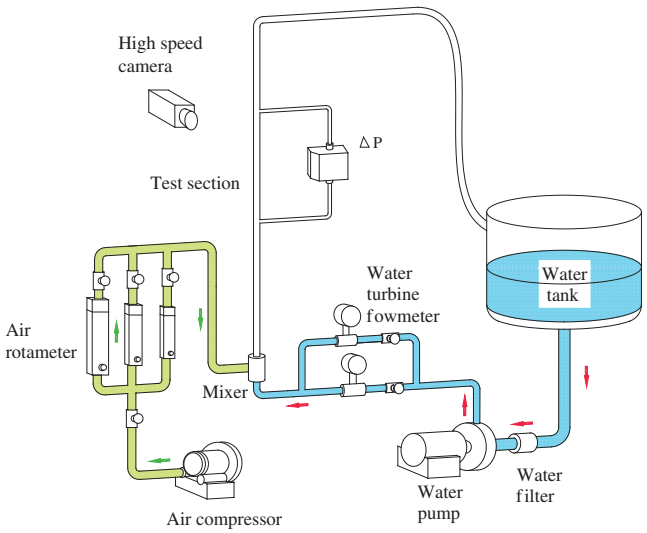

Fig. 4. The experiment setup.

Fig. 6 shows the flow pattern map in the 15.7 mm diameter tube. The transition boundaries of flow patterns were marked according to Butterworth and Hewitt [12]. The measured flow patterns generally match those reported by Butterworth and Hewitt [12].

4.2. Flow pattern modulation by the mesh cylinder

Fig. 7 shows the trajectories of miniature bubbles when they interact with the mesh cylinder. Three bubbles were selected. It is found that no matter where are the miniature bubbles initially, they enter the annular region finally. The mesh pore surface prevents the bubbles from entering the core region. These bubbles may change their flow directions and attack the flat bottom mesh surface. They flow in the annular region finally. The annular region ensures densely populated bubbles or early coalescence of the bubbles, creating flow disturbance to enhance heat transfer. The bubbly flow occurs at the liquid superficial velocity of 2.394 m/s (see Fig. 7). Bubbles are accelerating when they approach the mesh cylinder bottom and they may break into small ones due to the inertia force during the accelerating process.

Fig. 8 shows the modulation for cap or slug bubbles. The segmented gas–liquid flow is maintained in the annular region. Bubbles are in the elongated-ring-slug-bubble shape. The core region is full of liquid.

The reason of bubbles not entering the core region was analyzed by the surface energy. Fig. 9 considers a large bubble with its diameter identical to the tube penetrating a rectangular mesh pore. Tsai and Lin [13] gave the surface pressure increase when a bubble travels from the state A to state B as

$$P_1 - P_2 = 4\sigma\cos\alpha\left(\frac{1}{w} - \frac{1}{D}\right) \tag{2}$$

where w is the mesh pore width (0.15 mm here), D is the tube diameter and α is the contact angle for the bubble on the mesh pore surface.

For a bubble penetrating from the annular region to the mesh pore, the surface energy increase is

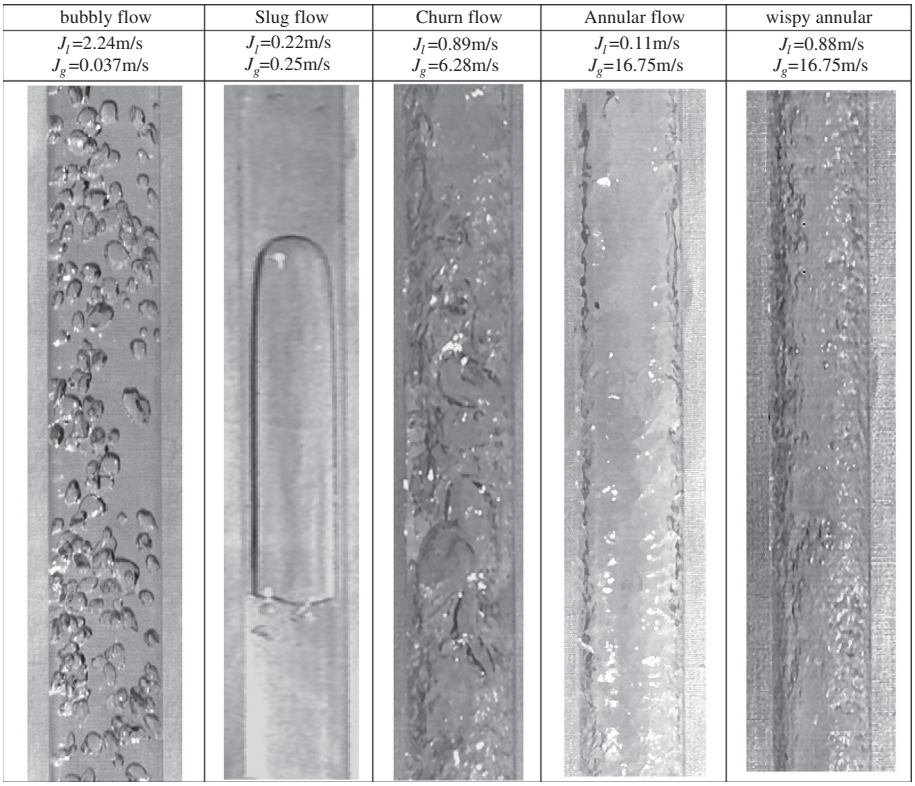

Fig. 5. Flow patterns observed in the vertical bare tube.

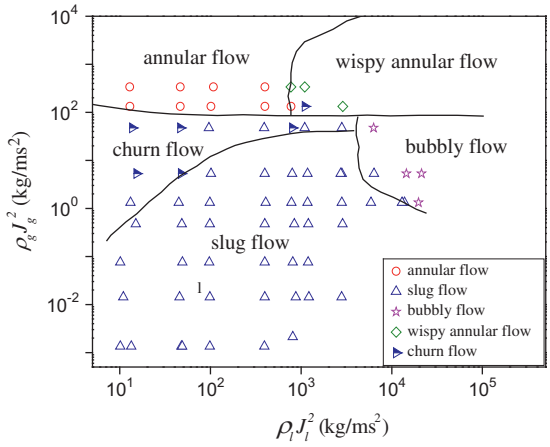

Fig. 6. The flow pattern map and comparison with Butterworth and Hewitt (1985), noting that data points are obtained by this study, solid lines were cited from Butterworth and Hewitt (1985).

$$P_1 - P_2 = 4\sigma\cos\alpha\left(\frac{1}{w} - \frac{1}{W}\right) \tag{3}$$

ere W is the annular gap size (2.65 mm here). The second term of the right side of Eqs. (2) and (3) contributes less to the pressure difference due to $D \gg w$ and $W \gg w$. $P_1 - P_2$ equals to 970 Pa for air/water system with $\sigma = 0.07275$ N/m (20 °C), $\alpha = 60°$ and $w = 0.15$ mm. Thus, the pressure difference should be more than ~1 KPa to penetrate the front bubble into the mesh pores.

4.3. The liquid film thickness on the wall surface

The heat transfer coefficient is directly inverse to the liquid film thickness, i.e., $h = k_l/\delta$, where k_l is the liquid thermal conductivity and δ is the liquid film thickness. Fig. 10a shows a cap bubble approaching and interacting with the mesh cylinder. The two-phase superficial velocities were $J_l = 0.115$ m/s and $J_g = 0.046$ m/s. Fig. 10b shows the tracking bubble with its length of 15.1 mm and traveling velocity of 0.35 m/s in the bare tube section. The liquid thicknesses were 4.62 mm, 2.39 mm and 0.82 mm at the three locations from the bubble nose to the bubble tail. Fig. 10c shows the same bubble in the annular region with its length of 24.07 mm. The bubble tightly contacted with the inner wall surface. The liquid film thickness was decreased to about 0.5 mm in the bubble body. Fig. 11a shows a slug bubble flowing in the bare tube section with $J_l = 0.43$ m/s and $J_g = 0.115$ m/s. The liquid film thicknesses were $\delta_1 = 3.73$ mm, $\delta_2 = 2.06$ mm and $\delta_3 = 1.19$ mm at the three locations. When the same bubble was flowing in the annular region, the liquid film thickness was so thin that it was difficult to be identified by the image system (see Fig. 11b).

There are two factors to cause the significant decrease of the liquid thickness in the annular region. The first factor is the miniature gap of the annular region. Taylor [14] obtained the liquid film thickness from the difference of the bubble velocity and the mean velocity over a wide capillary number range, experimentally. It is found that δ is increased with increases in capillary numbers and approaches a certain fraction of the tube diameter. Aussillous and Quere [15] correlated the Taylor's experimental data and gave the following expression:

$$\frac{\delta}{D} = \frac{0.67Ca^{2/3}}{1 + 3.35Ca^{2/3}} \tag{4}$$

where D is tube diameter, Ca is the capillary number ($Ca = \mu_l U/\sigma$), where μ_l is the liquid viscosity, U is the bubble velocity. Eq. (4) is called the Taylor's law.

The liquid film thicknesses were compared in the bare tube and annular region. Giving $D = 15.7$ mm and $d = 10.4$ mm (mesh cylinder diameter), the effective diameter of the annular region is

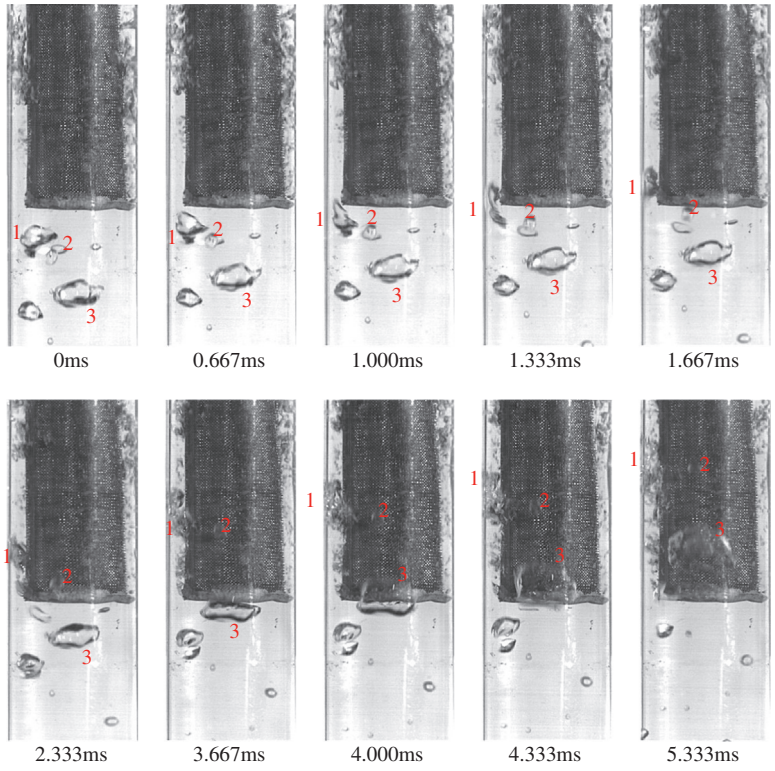

Fig. 7. The transient process of miniature bubbles entering the annular region (J_l = 2.394 m/s, J_g = 0.029 m/s, x_s = 985 mm, x_e = 1122 mm, x_s and x_e represent the starting and ending locations of the visualization area along the flow direction).

$$D_{eff} = \frac{4A_a}{\pi(D+d)} = D - d \tag{5}$$

where A_a is the cross sectional area of the annular region. Having D_{eff} of 5.3 mm, which is about one-third of D, the liquid film thickness in the annular region should be one-third of that in the bare tube, assuming the same capillary numbers in both sections. Therefore, the heat transfer coefficient by the flow pattern modulation should be three times of that in the bare tube.

The other factor to influence the liquid film thickness is the bubble acceleration in the annular region. Han and Shikazono [9] measured local and instantaneous liquid film thickness under adiabatic conditions with laser focus displacement meter. They studied the effect of inertia force on the liquid film thickness using several working fluids in microchannels of different sizes, and proposed empirical correlations based on capillary number, Reynolds number and Weber number. The effect of bubble acceleration on liquid film thickness was studied by Han and Shikazono [10]. The increase of liquid film thickness with capillary number was suppressed when bubble acceleration is large, which was explained as that liquid film thickness was decreased due to the flow acceleration affecting the curvature between the bubble nose and transition region. Figs. 10 and 11 show that confinement of gas bubbles in the annular region causes the bubble acceleration to further reduce the liquid film thickness.

4.4. The flow structure

Fig. 12a and b shows the flow picture and three-dimensional drawing. The flow structure is summarized as follows:

(a) The elongated-ring-slug-bubbles sweep the annular region periodically with higher velocities. The bubbles are segmented by liquid plugs.

(b) The core region is full of liquid. When a ring slug bubble sweeps the annular region, the core region has the downward flow. Alternatively, when a liquid plug sweeps the annular region, the core region has the upward flow. Thus, the pulsating flow is self-sustained in the core region.

(c) The mesh pores promote the liquid mass and momentum exchange across the two sides of the mesh cylinder.

Fig. 12c illustrates the flow picture in the $r - x$ two-dimensional plane, where r is the radial coordinate and x is the axial coordinate. In the annular region, the slug bubble length was L_s and the liquid plug length was L_l. Four specific points of A, B, C and D were selected, in which A and B were at the center of two neighboring slug bubbles in the flow direction. The point A was in the annular region and B was in the core region. Points C and D were at the same height, in which C was in the core region and D was at the bubble front close to mesh pores. P_A and P_D have the following relationship by neglecting the frictional pressure drop in the flow direction and the pressure difference caused by the interface curvature at the slug bubble tail.

$$P_A = P_{D^+} + \rho_g g L_s + 0.5\rho_l g L_l \tag{6}$$

where P_{D^+} is the pressure at the gas side of the point D. Similarly, P_B and P_C have the expression of

$$P_B = P_C + \rho_l g(L_s + 0.5L_l) \tag{7}$$

Assuming no pressure gradient in the liquids along the radial direction, we have

$$P_A = P_B \text{ and } P_{D^-} = P_C \tag{8}$$

where P_{D^-} is the pressure at the liquid side of the point D. Combing Eqs. (6)–(8) yields

$$P_{D^+} - P_{D^-} = \Delta P_{buoyancy} = \Delta\rho g L_s \tag{9}$$

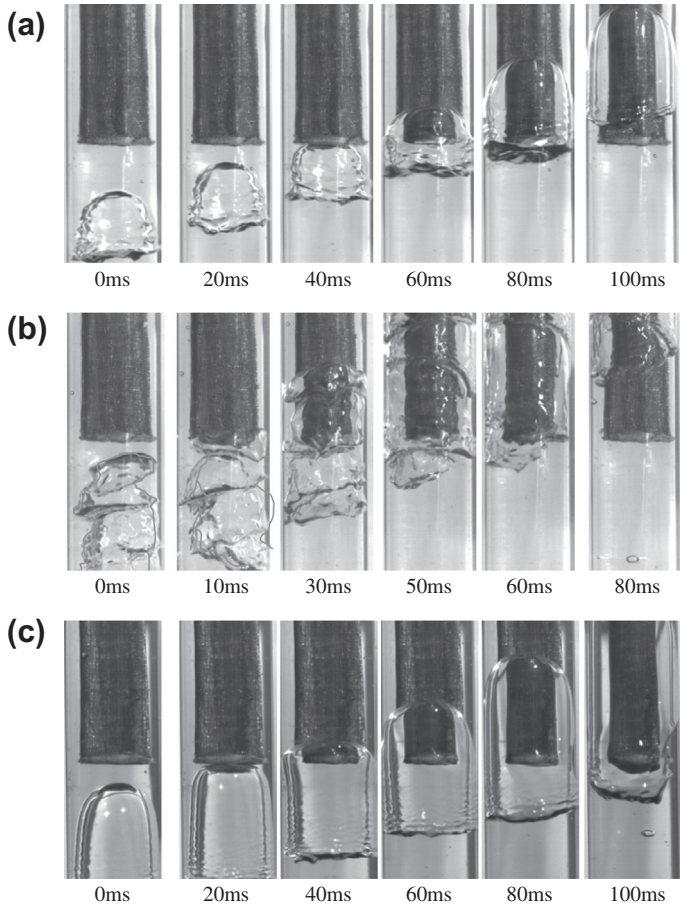

Fig. 8. The transient formation of elongated-ring-slug bubbles in the annular region (photos are taken from $x_s = 975$ mm and $x_e = 1030$ mm, a: $J_l = 0.115$ m/s, $J_g = 0.046$ m/s, b: $J_l = 0.215$ m/s, $J_g = 0.037$ m/s, c: $J_l = 0.057$ m/s, $J_g = 0.029$ m/s).

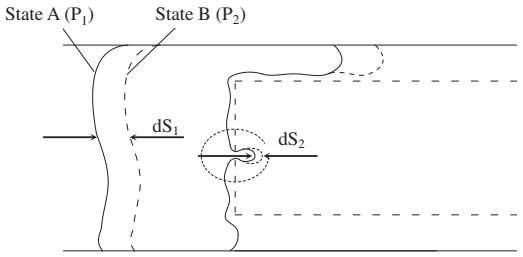

Fig. 9. Large bubble surface energy required to prevent the bubble from entering the mesh cylinder.

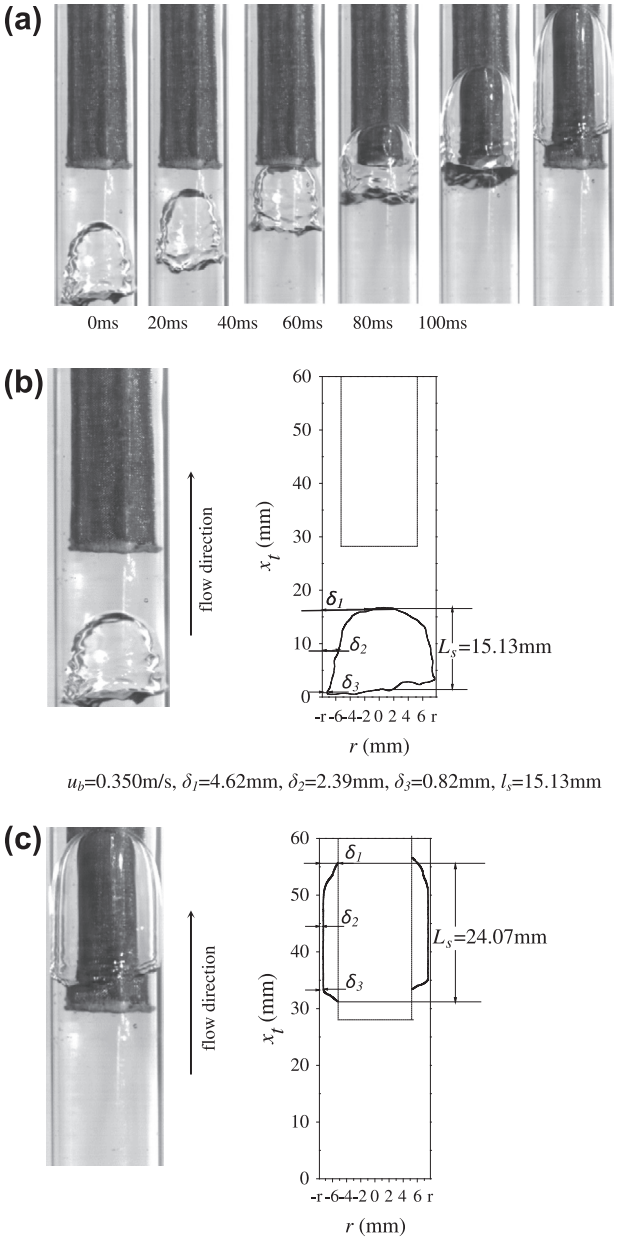

Fig. 10. The liquid film thickness in the bare tube and annular region ($x_s = 975$ mm, $x_e = 1025$ mm, $J_l = 0.115$ m/s, $J_g = 0.046$ m/s, x_t is the locally attached coordinate along the flow direction).

where $P_{D^+} - P_{D^-}$ is the pressure difference across the gas–liquid interface at the point D, which is caused by the buoyancy force between liquid in the core region and gas in the annular region, $\Delta\rho$ is the density difference of liquid and gas. Physically, $\Delta P_{buoyancy}$ should be balanced by the capillary force (ΔP_σ). The bubble breaks through the mesh pores at the point D if $\Delta P_\sigma < \Delta P_{buoyancy}$. Thus, the criterion for the initial bubble rupture is

$$\Delta\rho g L_s = \frac{4\sigma\cos\alpha}{w} \tag{10}$$

In terms of Eq. (10), the maximum slug bubble length to keep the bubble completeness is

$$L_{s,\max} = \frac{4\sigma\cos\alpha}{\Delta\rho g w} \tag{11}$$

Giving $\sigma = 0.072$ Nm at the room temperature, $\alpha = 60°$, $w = 0.15$ mm, $L_{s,\max}$ is 98 mm.

The average bubble lengths in the bare tube section and the annular region were measured to verify Eq. (11). Fig. 13 shows the bubble lengths, in which the open symbols for the bare tube section data and the solid symbols for the annular region data. C refers to the critical state to keep the slug bubble completeness in the annular region, beyond which a ring slug bubble will be broken at the bubble nose. The measured critical bubble length in the annular region was 86 mm at $J_l = 0.115$ m/s, slightly shorter than the value of 98 mm given by Eq. (11). The critical bubble lengths are shortened to about 49 mm at the liquid superficial velocities of 0.215 m/s and 0.430 m/s, indicating the bubble rupture not only governed by the buoyancy force, but also by the inertia force of the liquid. Eq. (11) tells us that a smaller mesh pore size maintains a longer bubble length to keep its completeness.

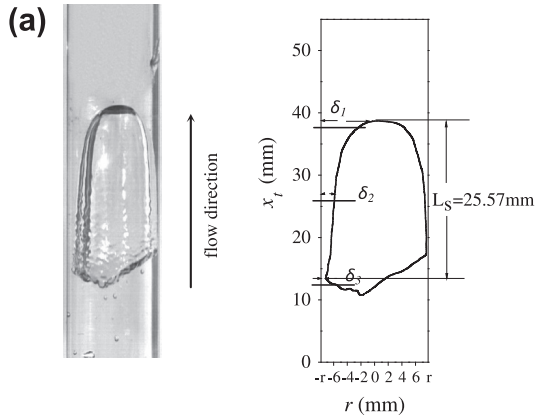

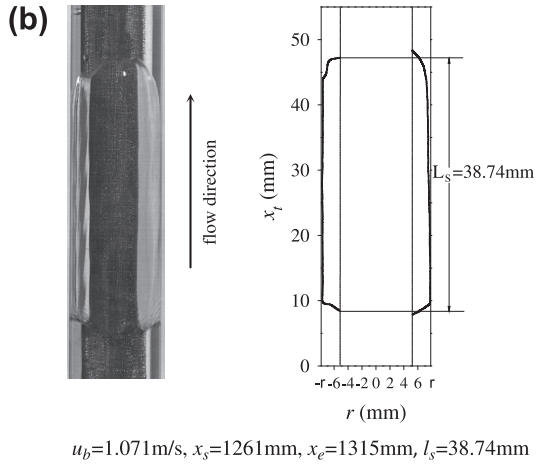

Fig. 11. The liquid film thickness in the bare tube and annular region (J_l = 0.430 m/s, J_g = 0.115 m/s).

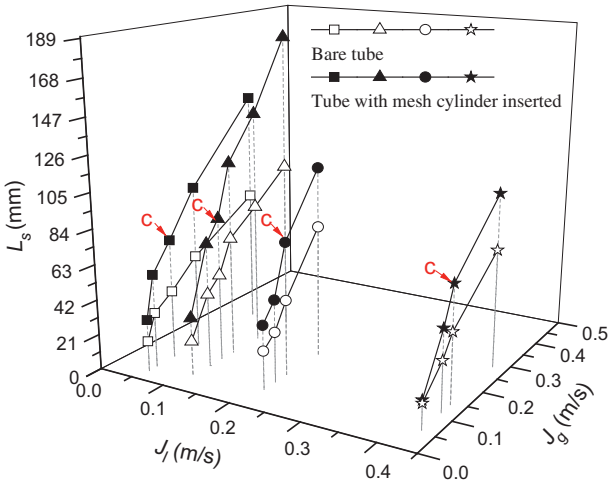

Fig. 13. The bubble lengths in the bare tube (open symbol) and the annular region (solid symbol) with J_l = 0.057 m/s, $L_{s,c}$ = 72 mm; J_l = 0.115 m/s, $L_{s,c}$ = 86 mm; J_l = 0.215 m/s, $L_{s,c}$ = 49 mm; J_l = 0.430 m/s, $L_{s,c}$ = 48 mm).

Fig. 14 shows the flow structures without and with bubble rupture. The bubble length influences the bubble rupture. The bubble length depends on J_l and J_g. Fig. 14a shows the complete bubble case with a shorter bubble length of 53 mm at J_l = 0.057 m/s and J_g = 0.086 m/s. But Fig. 14b shows the bubble rupture case with a longer bubble length of 91 mm. Miniature bubbles are separated from the mother slug bubble and entered the core region. Thus, they are seen at the tube exit.

Fig. 15 gave the experimental evidence that once the bubble rupture happens, the rupture location should be the bubble front close to the mesh pore surface (see the point *D* in Fig. 12). That location is the weakest to sustain the drag force created by the density difference between liquid in the core region and gas in the annular region.

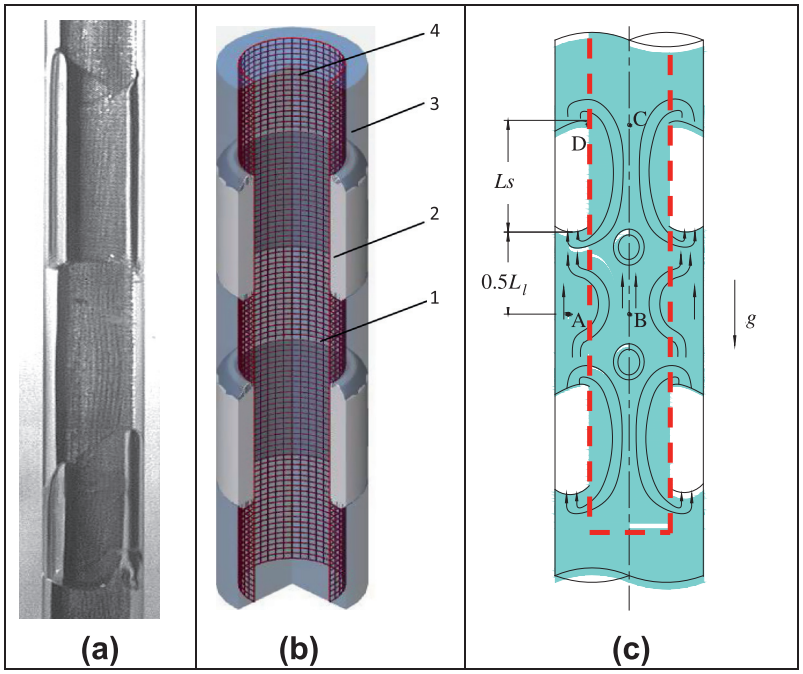

Fig. 12. The flow structure in the heat transfer tube (a: photo of the elongated-ring-slug-bubble, b: three-dimensional drawing of the flow structure with 1: mesh pore surface, 2: ring-slug-bubble in the annular region, 3: liquid plug in the annular region and 4: liquid in the core region, c: two-dimensional drawing of the flow structure).

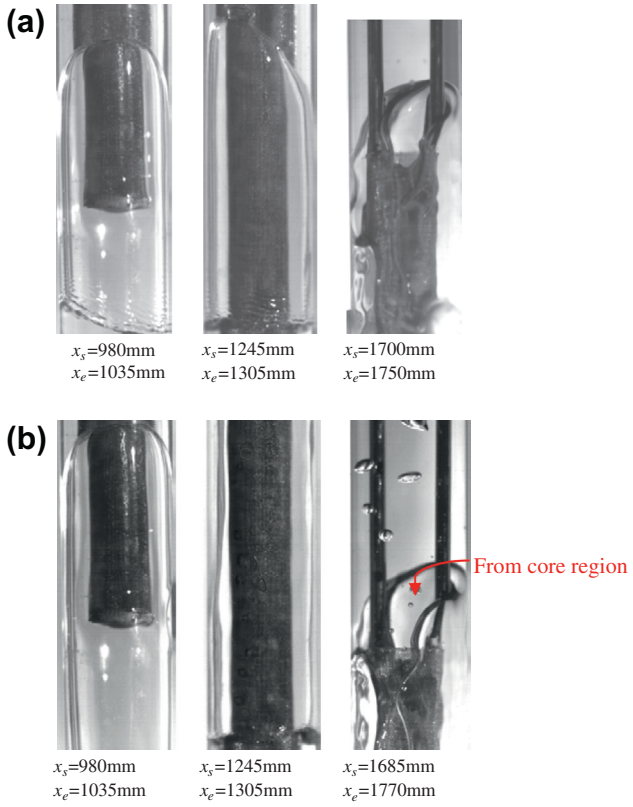

Fig. 14. The bubble in the entrance, middle and outlet regions of the mesh cylinder (a for the complete bubble case with L_s = 53 mm; and b for the bubble breaking case with L_s = 91 mm, both cases with J_l = 0.057 m/s and J_g = 0.086 m/s).

The miniature bubble leakage towards the core region does not influence the heat transfer enhancement. This is because the slug bubble lengths are almost identical before and after the miniature bubble emission. In addition, the miniature bubbles are very sparsely populated in the core region. For the boiling heat transfer, the liquid is changed to vapor. The vapor bubble in the core region does not influence the evaporation heat transfer enhancement. For the condensation heat transfer, the miniature bubbles in the core region can be fully condensed.

4.5. Buoyancy force induced pulsating flow

The pulsating flow can be self-sustained in the core region, which is a potential to be the second mechanism to enhance heat transfer. The pulsating flow does exist for complete slug bubble condition and bubble rupture condition. For the bubble rupture case, the miniature bubble separated from its mother bubble can be acted as the tracing particle to observe the pulsating flow.

Fig. 16 shows the miniature bubble trajectory marked by the red array. During the period of t = 0–60 ms, the liquid plug sweeps the annular region with the miniature bubble going up in the core region, causing the co-current flow in the annular region and core region. The upflow is sustained until at t = 120 ms. During the period of t = 120–225 ms, the counter-current flow is sustained with the gas upflow in the annular region and the liquid downflow in the core region. The flow direction in the core region is periodically changed to cause the pulsating flow. Fig. 17 plots the tracing bubble displacement versus time along the flow direction. A quasi-sine displacement curve is identified. For the time of t > 450 ms, the tracing bubble is out of the visualization zone thus the displacement curve ends.

The pulsating flow is helpful for the heat transfer enhancement. The mixing process between the annular region and core region enhances the liquid mass and momentum exchange across the mesh pore surface. The pulsating flow velocity of liquid in the core region is roughly estimated as

$$\Delta\rho g L_s = \frac{1}{2}\rho_l U_p^2 \tag{12}$$

Based on Eq. (12), the pulsating flow velocity is

$$U_p = \sqrt{\frac{2\Delta\rho g L_s}{\rho_l}} \tag{13}$$

The liquid mass exchange between the annular region and core region around a single slug bubble is

$$m_p = A_{mesh\text{-}cylinder}\sqrt{2\Delta\rho\rho_l g L_s} \tag{14}$$

where $A_{mesh\text{-}cylinder}$ is the total mesh pore area over a slug bubble height. Eqs. (13) and (14) show that the pulsating velocity and flow rate are changed with L_s by the $L_s^{0.5}$ law. For a slug bubble length of 80 mm, the pulsating flow velocity reaches 1.25 m/s.

The pulsating flow generated by the active pump was reported in the literature to enhance the heat transfer. Jin et al. [16] studied the active heat transfer enhancement by pulsating flow in a triangular grooved channel over the ranges of $270 < Re < 910$ and $0.08 < St < 0.67$ experimentally, where Re is the Reynolds number and St is the Strouhal number. The measured heat transfer was improved up to 350% at Re = 270 and St = 0.34 compared with the steady flow. The PIV results show that the heat transfer enhancement results from the strong mixing caused by the repeating sequence of vortex generation, growth, expansion and ejection from the groove to the main stream by the pulsating flow. The fluid

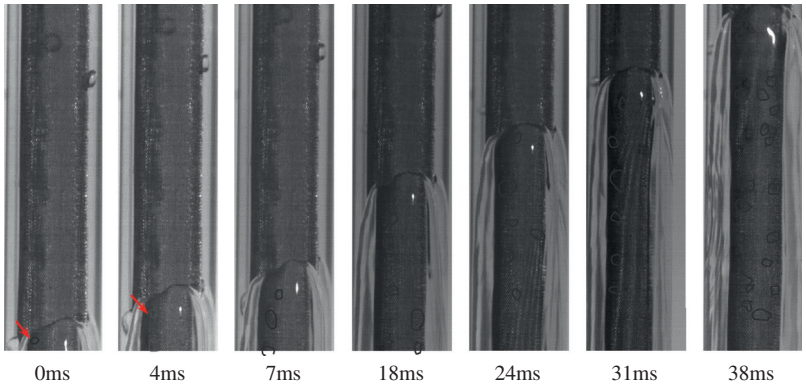

Fig. 15. The transient bubble breaking process (x_s = 1245 mm, x_e = 130 mm, J_l = 0.057 m/s, J_g = 0.086 m/s).

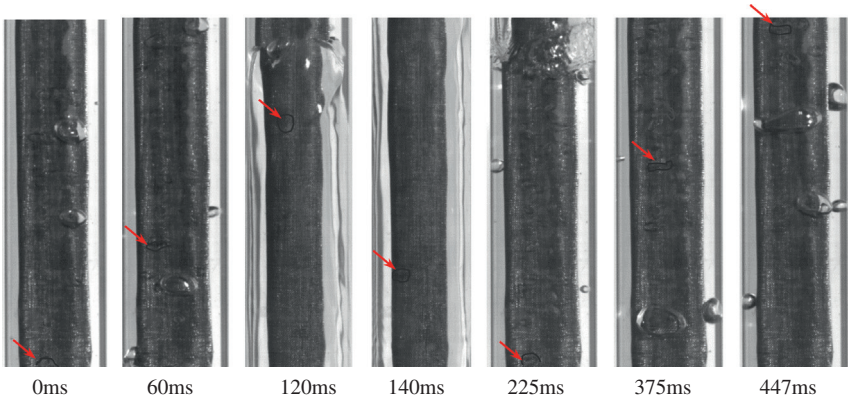

Fig. 16. The trajectory of the miniature bubble, identifying the buoyancy force induced pulsating flow in the core region (J_g = 0.115 m/s, J_l = 0.144 m/s, x_s = 1245 mm, x_e = 1315 mm).

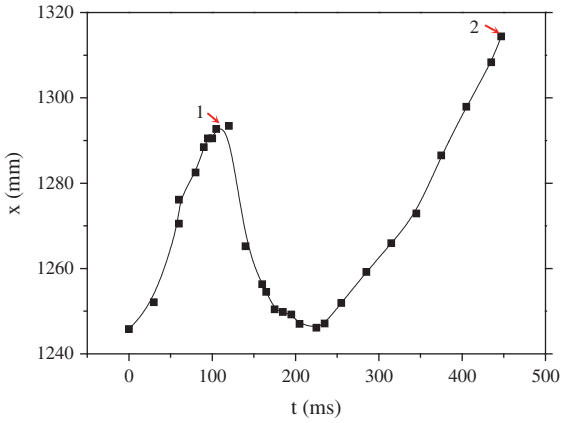

Fig. 17. The tracing bubble displacement in the core region with J_g = 0.115 m/s and J_l = 0.144 m/s.

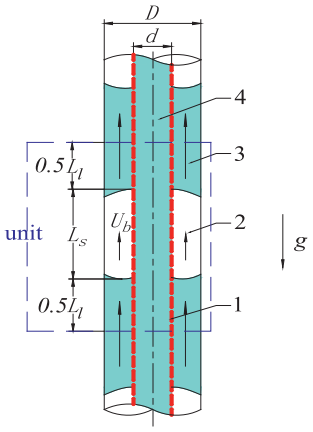

Fig. 18. The flow picture used to compute the liquid separation ratio.

mixing enhancement is maximized when the pulsation period matches the time duration for the vortex to grow large enough to fill the groove and then to be ejected to the main stream.

4.6. Comments on the flow pattern modulation for vertical upflow

This study proposed the flow pattern modulation concept, which has the potential to enhance the multiphase heat transfer. The key point is to ensure the bubbles flowing in the annular region. The following criteria should be kept to achieve this target.

4.6.1. The characteristic size ratio

To prevent bubbles from entering the core region, there should be a large surface energy increase when a bubble interacts with the mesh pores. Eq. (3) tells us that the surface energy criterion can be satisfied if the annular gap size is significantly larger than the mesh pore size. The size ratio of W/w is suggested to be at least 10 (i.e. $W/w > 10$), where W is the annular gap size and w is the mesh pore width.

4.6.2. The hydrophilic mesh screen surface

A hydrophilic mesh screen surface with the contact angle less than 90° is necessary to ensure the liquid flowing towards the core region and prevents the gas entering the core region.

4.6.3. The buoyancy forced induced criterion

A longer ring-slug-bubble in the annular region creates a larger pressure difference induced by the liquid and gas density difference. Eq. (11) gives the criterion that the mesh pore size is inversely proportional to the slug bubble length in the annular region. Thus, a smaller mesh pore size is needed to maintain the completeness for a longer slug bubble. The mesh pores had width of 150 μm in this study. More fined mesh pores will sustain much longer slug bubble length.

The flow pictures are significantly different between tubes with a mesh cylinder inserted and a solid block inserted. Inserting a solid block in a tube creates the thin liquid films on the tube wall but does not change the void fractions in the tube annulus in comparison to the bare tube. The mesh cylinder modulated flow increases the void fractions near the tube wall, generate thin liquid films on the wall and create the self-sustained pulsating flow. These benefits are expected to enhance the heat transfer and cannot be obtained by just inserting a solid block inside.

Even though the pulsating flow is self-sustained, the net liquid flow does exist in the core region. It is observed that the general trend of the tracking bubble displacement is increased with a set of pulse cycles passed. The maximum displacement was x = 1293 mm for the first cycle, but the observed displacement ends at x = 1315 mm for the second cycle (see points 1 and 2 in Fig. 17). The maximum displacement for the second cycle should be significantly larger than that at point 2. Comparing bubble displacements at points 1 and 2 directly illustrates the net liquid flow in the core region.

We define the liquid separation ratio, η, as the liquid flow rate in the core region divided by the total liquid flow rate. Fig. 18 is the flow picture to compute η based on the measured L_s (ring-slug-bubble length in the annular region), L_l (liquid plug length in the annular region), and U_b (bubble velocity). A flow unit

Table 1
The liquid separation ratio by the mesh cylinder.

Q_l (m^3/h)	Q_g (m^3/h)	J_l (m/s)	J_g (m/s)	L_s (mm)	L_l (mm)	U_b (m/s)	$\beta_{l,a}$	η
0.04	0.02	0.057	0.028	56	214	0.048	0.793	0.669
0.08	0.032	0.115	0.046	35	186	0.077	0.842	0.718
0.15	0.04	0.215	0.057	38	125	0.094	0.767	0.833
0.15	0.06	0.215	0.086	49	147	0.140	0.750	0.757
0.30	0.04	0.430	0.057	17	170	0.091	0.909	0.904
0.30	0.08	0.430	0.115	48	218	0.184	0.819	0.825

consists of a complete ring-slug-bubble and two half liquid plugs. The liquid volume fraction in the annular region is

$$\beta_{l,a} = \frac{A_a L_l}{A_a(L_s + L_l)} = \frac{L_l}{L_s + L_l} \tag{15}$$

The liquid volume flow rate in the annular region is

$$Q_{l,a} = \frac{\pi}{4}(D^2 - d^2)U_b\beta_{l,a} \tag{16}$$

Therefore, the liquid separation ratio is

$$\eta = \frac{Q_{l,c}}{Q_l} = \frac{Q_l - Q_{l,a}}{Q_l} = 1 - \frac{\pi(D^2 - d^2)U_b L_l}{4Q_l(L_s + L_l)} \tag{17}$$

where $Q_{l,c}$ is the liquid volume flow rate in the core region and Q_l is the total liquid volume flow rate. Eq. (17) obtains η with the measured parameters of U_b, L_l, L_s and Q_l, in which the former three parameters are processed using the observed image files and the last one is measured by the liquid flowmater. Table 1 shows the liquid separation ratios at various conditions. Over the data range given in Tab.1, the minimum and maximum liquid separation ratios are 66.9% and 90.4%, respectively. These data indicates that more than half of the liquid flows in the core region. The mesh screen surface does act the liquid separator function.

5. Conclusions

The passive phase separation concept was proposed to modulate flow patterns for vertical upflows. The tube is divided into an annular region and a core region, separated by a suspended mesh cylinder. Gas flows in the annular region and liquid flows in the core region. Due to the thin liquid films on the tube wall, the concept has the potential to enhance the multiphase heat transfer. Air/water two-phase flow experiments were performed. Miniature bubbles are modulated to flow in the annular region. Cap and slug bubbles are modulated to form the elongated-ring-slug bubble train in the annular region. The core region is full of liquid. The pulsating flow is self-sustained in the core region due to the large density difference across the two sides of the mesh pore surface. The liquid mass and momentum exchange is promoted by the mesh pore surface. For long slug bubble in the annular region (such as >10 cm), miniature bubbles are emitted from the bubble front. The emitted miniature bubble is treated as the tracking particle to directly observe the pulsating flow in the core region.

Acknowledgements

This work was supported by the Natural Science Foundation of China of International cooperation project (51210011), the Natural Science Foundation of China (51106050) and the National Basic Research Program of China (2011CB710703).

References

[1] J.G. Collier, Convective Boiling and Condensation, Oxford university press, Washington, 1982.
[2] Q. Chen, J. Xu, H. Chen, A new design method for Organic Rankine Cycles with constraint of inlet and outlet heat carrier fluid temperatures coupling with the heat source, Applied Energy 98 (2012) 562–573.
[3] S. Laohalertdecha, S. Wongwises, The effects of corrugation pitch on the condensation heat transfer coefficient and pressure drop of R-134a inside horizontal corrugated tube, International Journal of Heat and Mass Transfer 53 (2010) 2924–2931.
[4] D. Graham, J.C. Chato, T.A. Newell, Heat transfer and pressure drop during condensation of refrigerant 134a in an axially grooved tube, International Journal of Heat and Mass Transfer 42 (1998) 1935–1944.
[5] A. Cavallini, D. Del Col, L. Doretti, G.A. Longo, L. Rossetto, Heat transfer and pressure drop during condensation of refrigerants inside horizontal enhanced tubes, International Journal of Refrigeration 23 (2000) 4–25.
[6] A. Miyara, Y. Otsubo, Condensation heat transfer of herringbone micro fin tubes, International Journal of Thermal Sciences 41 (2002) 639–645.
[7] S. Lips, J.P. Meyer, Experimental study of convective condensation in an inclined smooth tube. Part I: Inclination effect on flow pattern and heat transfer coefficient, International Journal of Heat and Mass Transfer 55 (2012) 395–404.
[8] Y. Han, N. Shikazono, N. Kasagi, The effect of liquid film evaporation on flow boiling heat transfer in a micro tube, International Journal of Heat and Mass Transfer 55 (2012) 547–555.
[9] Y. Han, N. Shikazono, Measurement of the liquid film thickness in micro tube slug flow, International Journal of Heat and Fluid Flow 30 (2009) 842–853.
[10] Y. Han, N. Shikazono, The effect of bubble acceleration on the liquid film thickness in micro tubes, International Journal of Heat and Fluid Flow 31 (2010) 630–639.
[11] C. Fang, M. David, F.-M. Wang, K.E. Goodson, Influence of film thickness and cross-sectional geometry on hydrophilic microchannel condensation, International Journal of Multiphase Flow 36 (2010) 608–619.
[12] D. Butterworth, G.F. Hewitt, Two Phase flow and Heat Transfer, Oxford University Press, Beijing, 1977 (X.J. Chen translated).
[13] J.H. Tsai, L. Lin, Active microfluidic mixer and gas bubble filter driven by thermal bubble micropump, Sensors and Actuators A: Physical 97–98 (2002) 665–671.
[14] G.I. Taylor, Deposition of a viscous fluid on the wall of a tube, Journal of Fluid Mechanics 10 (1961) 161–165.
[15] P. Aussillous, D. Quere, Quick deposition of a fluid on the wall of a tube, Physics of Fluids 12 (2000) 2267–2371.
[16] D.X. Jin, Y.P. Lee, D.Y. Lee, Effects of the pulsating flow agitation on the heat transfer in a triangular grooved channel, International Journal of Heat and Mass Transfer 50 (2007) 3062–3071.